Coincident energy and angular distributions in Xenon $4d_{5/2}$ inner-shell double photoionization

M Wiedenhoeft†‡, S E Canton†§, A A Wills†||, T Gorczyca†, J Viefhaus‡¶, U Becker‡and N Berrah†

†Physics Dept., Western Michigan University, Kalamazoo, MI 49008, USA
‡Fritz-Haber-Institut der Max-Planck-Gesellschaft,14195 Berlin, Germany

E-mail: wiedenhm@gvsu.edu

Abstract. We report on measurements of the triply differential cross section for the $4d_{5/2}$ inner-shell photoionization in Xenon followed by $N_5O_{2,3}O_{2,3}$ Auger decay using electron-electron coincidence spectroscopy. The experimental setup made it possible to obtain the first coincident angular distributions for the $^1D_2$ and $^3P_2$ final states at a photon energy of 97.45 eV.

PACS numbers: 32.80.Fb, 32.80.Hd

Keywords: photoionization, inner-shell, Auger decay, double photoionization, xenon, γ-(2e), photo double-ioniztion, Submitted to: *J. Phys. B: At. Mol. Phys.*

1. Introduction

Photo double-ionization (PDI), the emission of two electrons resulting from single photon absorption, has been intensively studied by many research groups over the past two decades (Mazeau et al. 1991, Selles et al. 1998, Briggs and Schmidt 2000, Schwarzkopf et al. 1993, Dörner et al. 1998, Viefhaus et al. 1998, Viefhaus et al. 1996, Avaldi and Huetz 2005) since it is related to two important topics of modern atomic physics, namely electron correlations and the three-body Coulomb problem. Understanding the role of both effects in the PDI process can be achieved through a detailed description of the Triply Differential Cross Section (TDCS), $\frac{d\sigma^3}{dE_1 d\theta_1 d\theta_2}$, that can only be carried out through coincidence measurements between two of the ionization fragments.

In sequential PDI, such as the $4d_{5/2}$ inner-shell ionization in Xenon with subsequent $N_5O_{2,3}O_{2,3}$ Auger decay

$$\gamma + Xe \rightarrow Xe^+(4d_{5/2}^{-1}) + e_{pho} \rightarrow Xe^{2+}(5p^{-2}) + e_{Aug} \quad (1)$$

‡ Present address: Grand Valley State University, Allendale, MI 49401, USA
§ Present address: Dept. of Chemical Physics, University of Lund,SE-22100 Lund, Sweden
|| Present address: Manchester, United Kingdom
¶ Present address: Deutsches Elektronen-Synchrotron DESY, 22607 Hamburg, Germany

the singly charged intermediate 4d core hole can decay via an Auger process into a doubly charged final state. The two outgoing electrons are correlated via the intermediate state, and further through the final states under particular experimental conditions, such as both electrons having similar kinetic energy or ejection direction. Because electrons are indistinguishable, it is necessary to describe the Auger electron as a resonance embedded in the PDI continuum (Åberg 1980, Åberg and Howard 1982, Tulkki et al. 1987). The striking theoretical prediction within this model (Vegh 1994*a*, Vegh 1994*b*) of strong interference effects in the TDCS for the case when both free electrons have the same kinetic energies has caught researchers attention and was investigated experimentally in the valence outer-shell PDI of Neon (Schaphorst et al. 1996) and inner-shell PDI of Xenon (Schwarzkopf and Schmidt 1996, Viefhaus et al. 1998, Selles et al. 1998). Earlier experimental work (Selles et al. 1998) has also shown how the spin state determines the constructive or destructive nature of the interference, which is a consequence of a general selection rule (Maulbetsch and Briggs 1995) already verified in direct PDI of Helium (Schwarzkopf et al. 1993). With three charged particles in the final state, PDI requires in addition a detailed delineation of Coulomb interactions in the resulting few body system, also called Post Collision Interactions (PCI). The common manifestations of PCI in non-coincident measurements are significant shifts of the atomic lines whose tails also become asymmetric. These effects disappear in photoionization experiments when the difference in velocities between photo and Auger electron is large (Armen et al. 1987, Borst and Schmidt 1986). Recent studies (Lablanquie et al. 2001, Lörch et al. 2001, Scherer et al. 1999, Scherer et al. 2001, Rioual et al. 2001) of PDI have taken up the challenge posed by the most intricate kinematics conditions, where exchange effects and PCI effects are expected to both influence equally the angular dependency of the TDCS, in particular for the case of small relative angles and the small velocity difference of the two electrons (Scherer et al. 2001, Rioual et al. 2001). Recently, the reduction of the TDCS for small angle in the angular distribution of $^1S_0$ final state of the Xenon $N_5O_{2,3}O_{2,3}$ decay was reported (Scherer et al. 2004). Although two further angular distributions of the TDCS for photoelectron and Auger electron in Xenon have been shown (Selles et al. 1998), recent angular distribution measurement concentrated on double Auger decay processes (Viefhaus et al. 2004, Viefhaus et al. 2005).

Based on this motivation, we report here on the first kinetic energy and angular distributions for the Auger decay from Xenon $4d_{5/2}$ photoionization leading to $^3P_2$, $^1D_2$ final state of the $N_5O_{2,3}O_{2,3}$ Auger decay. We also show that it is possible to adequately describe these coincident angular distributions using a two-step model approach. Furthermore, the angular distribution data allows one to extract some information about the amplitude and phases of the emitted Auger electron and photoelectrons, see for example Kämmerling et al.(1993), Schaphorst (1997). Although our experiment is not meant to deliver precise and absolute values.

We present in section 2 the method for coincident data collection and data analysis and in section 3.1the coincident energy distributions. Section 3.2 discusses the angular distributions of the photoelectron and the angular distributions of the Auger electron when one of these two electrons is detected along the polarization vector of the incident light. At the end of

section 3.2 we estimate the amplitude and phases of the emitted electrons from the angular distribution results.

2. Experimental method and data analysis

The experiment was performed at the high resolution Atomic Molecular and Optics Beamline 10.0.1 at the Advanced Light Source (ALS) in Berkeley, CA. The experiments were conducted during the timing (double bunch) mode of the synchrotron operation. Figure 1 shows the

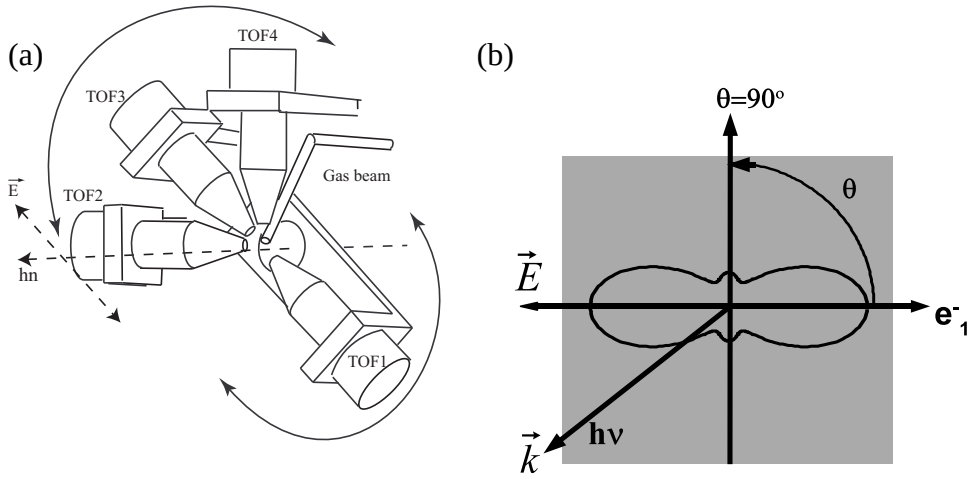

Figure 1. Schematic of (a) the experimental set up (see text), and (b) the angle notation used here.

schematic of the experimental apparatus. It consists of a set of 4 rotating electron time-of-flight (TOF) energy analyzers, which are well suited to perform coincident measurements where the kinetic energy of the two emitted electrons spreads out over a wide kinetic energy range. The 4 TOF analyzers are placed in a plane perpendicular to the direction of the incident light which crosses an effusive gas beam. Mechanical constraints (size of the vacuum vessel) limit the length of the drift tube of the analyzers to 12.5 cm. This drift tube leads to a relative kinetic energy resolution of $\Delta E/E \approx 5\%$.The analyzer provides a higher detection efficiency with an acceptance angle of $d\Omega = 5^\circ$ (solid angle). The TOF drift tube has a two step potential to minimize lens effects when a retarding voltage is applied, improving the absolute energy resolution. For the measurements described here we applied a retarding potential, $V_{ret} = -28.5$ V. This resulted in an absolute energy resolution of about 75 meV for electrons with a kinetic energy of 30 eV and about 275 meV at 34 eV. The photon energy was set to $h\nu = 97.5$ eV, with a resolution of 50 meV. The total coincidence resolution ΔE_{coinc} may be be approximated by $\sqrt{\Delta E_1^2 + \Delta E_2^2}$. The analyzer labeled 'TOF1' in figure 1 can rotate independently from the rotation of the TOF analyzers 2-4. Thus it is possible to set any relative angle θ_{12} between TOF1 and the other three, the smallest angle possible being $\theta_{12} = 35^\circ$. The coincident data of each detector pair were recorded in a 2 dimensional map of the flight times of the electrons detected in TOF1 and TOF2 as x and y coordinates respectively, and the TDCS intensity in the z coordinate. Also, the non-coincident spectra for each analyzer were

recorded simultaneously. Commonly, the TDCS is presented as the angular dependence (θ_1) of the emission probability of one electron, when the kinetic energy and the angle of the second (θ_2) are fixed, rather than as energy distribution. An example and the notations of the coordinate system used is given in figure 1(b). The angle θ_1, θ_2 lie in the plane perpendicular to the propagation direction $\vec{k}$ of the light, with $\theta = 0^\circ$ in the direction of the polarization vector of the light. In order to extract an angular distribution pattern many measurements with several θ_{12} settings are necessary. During the different measurements TOF1 was held fixed at a 'reference' angle of $\theta = 0^\circ$ with respect to the polarization vector of the incident light. In this way several sets of three θ_{12} values ranging from $35^\circ - 180^\circ$ were taken successively, by varying the positions of TOF2-4. Each set had a recording time of 10,000 s to 20,000 s depending on the experimental conditions.

The kinetic energy scale associated with each TOF analyzer was calibrated by recording the

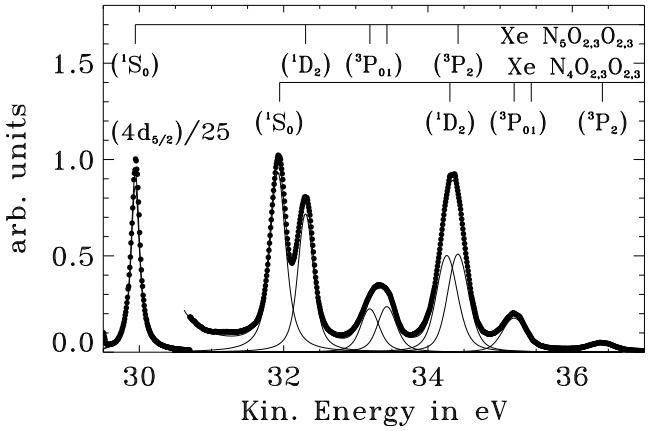

Figure 2. Non-coincident Xenon $N_{45}O_{23}O_{23}$ Auger spectrum recorded at a photon energy of 97.45eV after final time-to-energy conversion. The fit results (shown as thin lines) were needed to determine the nominal energies E_{pho} and E_{Aug}, in order to minimize uncertainties in the time-to-energy conversion of the time-of flight data.Note that at this photon energy the $4d_5/2$-photoline overlaps with the $^1S_0$ final state. The photoline is shown here, scaled down by 25

Neon 2s and 2p lines, having well known binding energies (NIST 2007), at various photon energies. The xenon time spectra were then converted to kinetic energy. In order to improve the precision of the time-to-energy conversion, the resulting energy spectra were then fitted with multiple Voigt profiles (see figure 2). The resulting energy values for the different photo lines and Auger lines were again compared with literature values. Significant deviations were incorporated in a corrected time-to-energy table and the improved conversion was performed again until a consistent conversion was found which finally showed an overall agreement within 30 meV in all cases.

During the experiment the partial pressure was kept below 1×10^{-5} Torr in order to keep the random coincident detection rate below an acceptable limit of the data handling electronics.

Random coincident detections are mostly due to electrons originating from two *different* atoms ionized by the same light pulse. To further process the data, the non-coincident spectra of the two analyzers involved were used to calculate the statistical random coincidence probability, taking into account the corresponding dead times of the analyzer electronics. These 'random' coincidences were then subtracted from the total coincidence data. The ratio of 'true' to 'random' coincidences was around $5-20\%$ depending on the angle pair in question. Since a retarding voltage of -28.5 V was applied, only the $4d_{5/2}$ photoelectrons and $N_{4,5}O_{2,3}O_{2,3}$ Auger electrons could be measured in coincidence (the kinetic energy of the Xe $4d_3/2$ photo line is just about 28eV at $h\nu = 97.45eV$). The vanishing (random) coincidences between $N_4O_{2,3}O_{2,3}$ Auger electrons and N_5 photoelectrons serve as a good indication of the quality of the random subtraction.
Finally, the analyzer transmission had to be considered. For TOF analyzers the transmission efficiency is a function of the electron kinetic energy. This function was calculated by comparing the measured ratio of Neon 2s over 2p photo lines as a function of the varied photon energy $h\nu$ to the literature values (Wuilleumier and Krause 1979). Neglecting effects due to differences in the effective source volume for the non-coincident and the coincident case respectively, the coincident transmission $Tr_{co}(E_1,E_2)$ can be calculated from non-coincident transmissions of TOF1 ($Tr_1(E_1)$) and TOF2 ($Tr_2(E_2)$) as follows:

$$Tr_{co}(E_1,E_2) = Tr_1(E_1)Tr_2(E_{,2}) \tag{2}$$

The applicability of the formula was verified by the comparison of coincident data measured in equivalent geometries.

3. Results and discussion

3.1. Energy distribution of the TDCS including Post-Collision Interaction Effects

In this section, we discuss the kinetic energy distributions of the triply-differential cross section (TDCS) for the final states of $(^1D_2)$ and $(^3P_2)$ of the doubly ionized Xenon following $4d_{5/2}$ photoionization. An example of our two-dimensional data, already converted to an energy axis, can be seen in figure 3(a) at the smallest relative angle $\theta_{12} = 35^\circ$. As it was pointed out before, the $4d_{3/2}$ photoelectron was prevented from reaching the detector due to the choice of retarding potential, so only the coincidences between the $4d_{5/2}$ photoelectron and the $N_5O_{2,3}O_{2,3}$ Auger electrons can be seen. The final states are from center bottom to top $(^1S_0)$ at 29.95 eV, $(^1D_2)$ at 32.3 eV, $(^3P_{0,1})$ -not resolved- and $(^3P_2)$ at 34.45 eV. The $^3P_2$ doubly charged final state data shown in figure 3(b) are obtained by integrating the intensities (over the width of the selected final state) along the points were the sum of the kinetic energies recorded in detector 1 and detector 2 is a constant and equal to the sum of the nominal energy of the Auger electron plus the energy of the photoelectron. In the absence of PCI effects, one would only measure a coincident signal at the nominal kinetic energies of the Auger electron and photoelectron. However in this case we clearly recorded a signal widely distributed along energies, where the sum of the two kinetic energies is a constant. The signals appears as the "horizontal lines" in figure 3 (a). This shows the main advantage of the time of flight

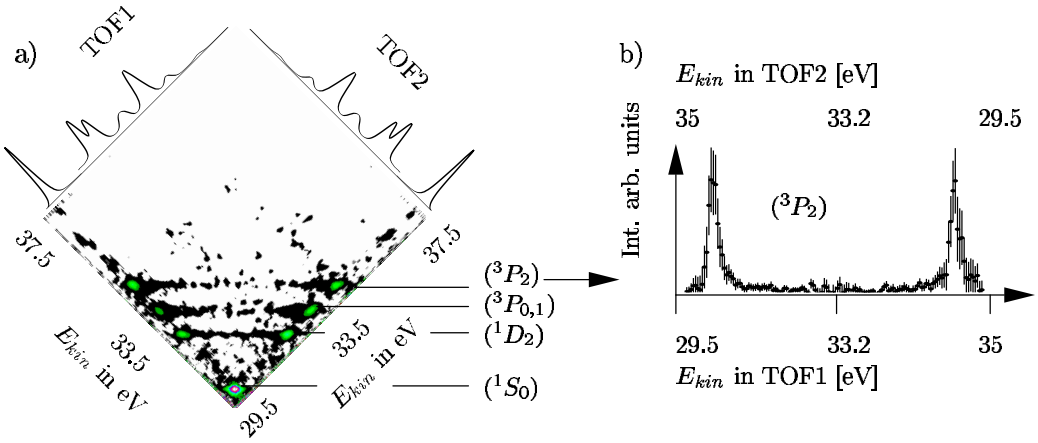

Figure 3. a) The 2D map of the coincidences in analyzer 1 and 2 illustrates the data handling (Lighter colour = higher intensity). The final states are from center bottom to top $(^1S_0)$ at 29.95 eV, $(^1D_2)$ at 32.3 eV, $(^3P_{0,1})$ -not resolved- and $(^3P_2)$ at 34.45 eV. b) A slice of the 2d-map intensity plotted vs E_{kin} of the electron detected in TOF1 [eV] for the final state $(^3P_2)$. *The left peak* shows the photoelectron in TOF1(35°) and the Auger electron in TOF2(0°), *the right peak* corresponds to the detection of the photoelectron in TOF2 and the Auger electron in TOF1.

technique that also electron intensities at "unexpected" energies (i. e. in between and off the nominal energies) are simultaneously recorded. In the measurements of the TDCS as a function of the kinetic energy of one of the electrons (see figure 3(b) the PCI effect manifests itself in an asymmetric line profile of the TDCS and some intensity between the two expected peaks.

In order to account for this PCI effect we use the formulation of the sequential PDI (Åberg 1980, Åberg and Howard 1982). According to Sheinerman and Schmidt (1997) the transition amplitude for the process of inner shell ionization and subsequent Auger decay can be given by:

$$T_{fi} = \frac{1}{\sqrt{2}} \sum \left[\frac{M_1(k_p) M_2(k_A)}{\varepsilon_A - \varepsilon^0_{Aug} + i\frac{\Gamma}{2}} R(A,p) - (-1)^S \frac{M_1(k_A) M_2(k_p)}{\varepsilon_p - \varepsilon^0_{Aug} + i\frac{\Gamma}{2}} R(p,A) \right] \tag{3}$$

Here $M_1(k_{p,A})$ is the amplitude of the inner shell ionization with an ejection of the (photo) electron of momentum k_p and a kinetic energy of ε_p, while $M_2(k_{p,A})$ describes the Auger decay, with kinetic energy ε_A and momentum k_A . Γ is the width of the intermediate state. The nominal energy of the Auger electron is denoted by ε^0_{Aug} . The factor $R(A,B)$ takes the PCI effect into account. The triply-differential cross section (TDCS) $\frac{d\sigma}{d\varepsilon_p d\theta_p d\theta_A}$ is found then by :

$$TDCS = 2\pi \left| T_{fi} \right|^2 \delta(h\nu - E^{2+}_{bin} - \varepsilon_p - \varepsilon_A) \tag{4}$$

In this presentation, the data were evaluated such that the sum of kinetic energies of the two emitted electrons equals the total excess energy E_{exc}, or

$$h\nu - E^{2+}_{bin} \equiv \varepsilon_p + \varepsilon_A \tag{5}$$

Hence the sum of the kinetic energies is a constant as is required by energy conservation. Equations (3),(4) then lead to the distribution of the TDCS as a function of the kinetic energy of one electron (eg ε_p), where the kinetic energy of the second electron (ε_A) is given by (5). When $\varepsilon_A - \varepsilon_p >> \Gamma$ one of the terms in (3) will become very small and interference effects will contribute only a small part. This result in two lorentzian like profiles around the nominal energy of the photoelectron when $\varepsilon_A = \varepsilon^0_{Aug}$ and $\varepsilon_p = \varepsilon^0_{pho}$ and having a FWHM of Γ. The intensity of the TDCS will depend on the amplitudes $M_{1,2}(k_{p,A})$, hence the momentum of each electron. The PCI effect as expressed in the factor R(A,B) will give rise to an asymmetric shape of the cross section, depending on the relative angle θ_{pA} and the energies of the photoelectron and Auger electron. In general, the TDCS for given θ_{pA} plotted as a function of the kinetic energy of one of the electrons will be approximately $Lorentzian(\varepsilon^{nom.}_{pho}, \Gamma) \times |R(p,A)|^2 + Lorentzian(\varepsilon^{nom.}_{Aug}, \Gamma) \times |R(A,p)|^2$. The numerical details of determining the PCI effect are found in the appendix.

To achieve reasonable statistics the measured intensities were added into kinetic energy intervals of 40 meV. During the first qualitative analysis the described equations were evaluated and then the theoretical TDCS was convoluted with a Gaussian to taking into account the photon energy resolution and the combined TOF analyzer resolutions. The calculated energy distribution was scaled in height to the data. In the range of interest, the precise determination of the analyzer resolution did not have a large impact to the outcome of the final line shape.

Figure 4 shows the results for selected $\theta_{12} = 35, 55, 159$ and 180°. The agreement in the line shape between theory and experiment is very good for the whole measured range of θ_{12}. Note, that in figure 4 *the left peak* shows the TDCS for the photoelectron in TOF1 and the Auger electron in TOF2, *the right peak* corresponds to the detection of the photoelectron in TOF2 and the Auger electron in TOF1. The x-axis is the kinetic energy of the electron detected in TOF1; energy conservation gives the kinetic energy of the second electron. It can be seen that the asymmetry in the TDCS changes direction when varying θ_{12} from 35° to 180°. For $\theta_{12} = 35^\circ$ the PCI effect is such that the center of the TDCS is shifting by about 40meV toward the point where the kinetic energy of both electrons is equal. That means that a fraction of the photoelectrons gain energy on - or from - the Auger electrons. For an angle θ_{12} greater than about 60° the asymmetry reverses, and hence the Auger electrons gain energy above their nominal kinetic energy, although much less pronounced by about 30meV, than for small relative angles. The change in the direction of the shift occurs for this data set at about $\theta_{12} = 55^\circ$, no PCI effect is visible (full and dashed lines in figure 4 coincide). It is for this angle that in (A.5) the parameter $K(v_1, v_2, \theta_{12}) = 1$ (since $C(v_1, v_2, \theta_{12}) = 0$), and also $|R(A,B)|^2 = 1$ in (A.6).

3.2. Angular distributions of the TDCS

Coincident angular distribution patterns between the photoelectron and Auger electron give experimental values for the underlying matrix elements and their relative phases, describing the correlation between the electrons during the inner shell photoionization and the subsequent

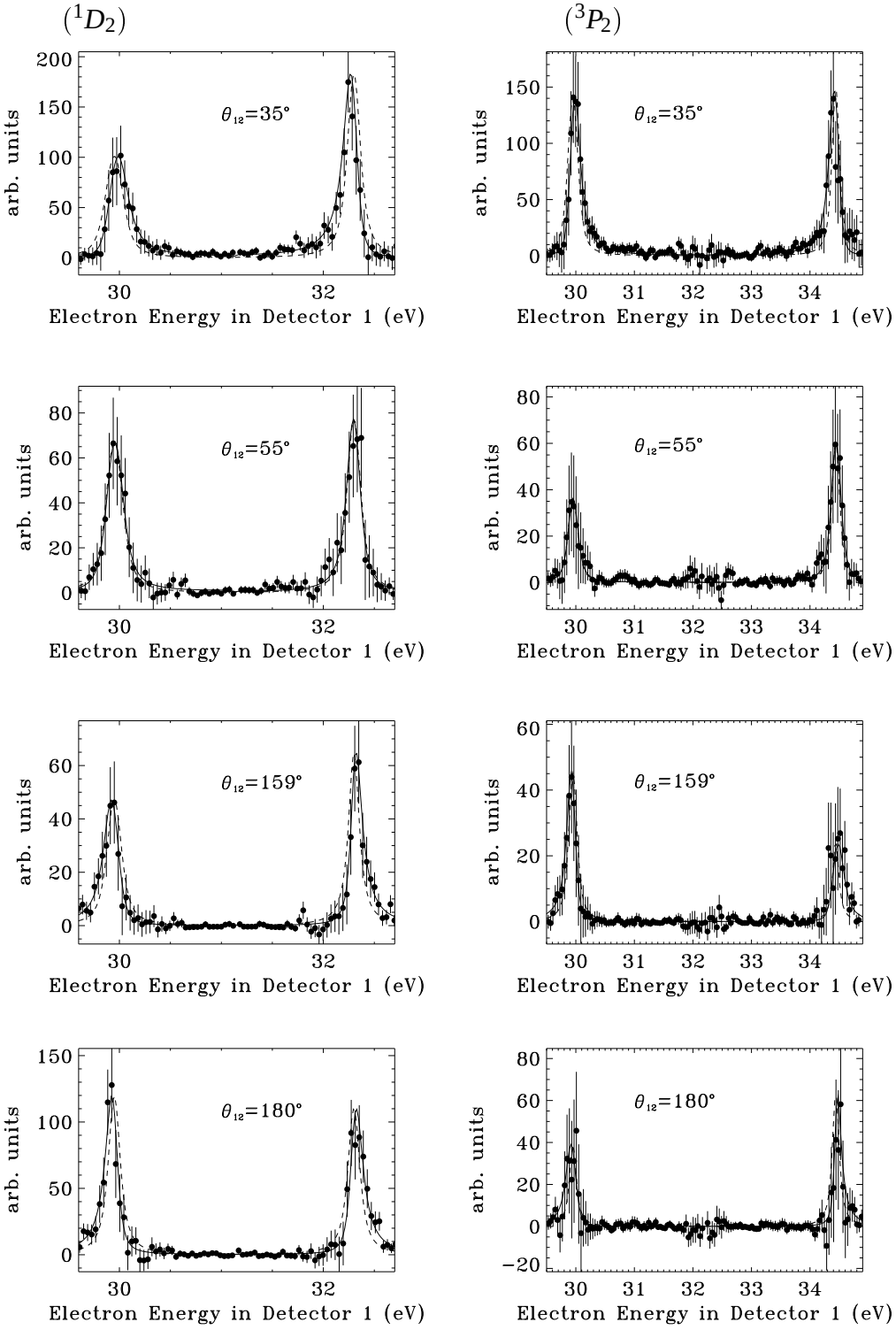

Figure 4. The energy distribution for various θ_{12} for the $(^1D_2)$ (left) and $(^3P_2)$ final states. The solid lines are scaled results from (A.1). The dashed lines show the non-PCI affected TDCS for comparison. θ_{12} from top to bottom: 35°,55°,159° and 180°. *The left peak* shows the TDCS for the photoelectron in TOF1 and the Auger electron in TOF2, *the right peak* corresponds to the detection of the photoelectron in TOF2 and the Auger electron in TOF1

Auger decay. As Schmidt pointed out - for example in (Schmidt 1999) - selecting processes where either the Auger electron (or photoelectron) is described by a single matrix element, one can study the photoionization (or the Auger decay) completely. This was demonstrated in the photoionization of Xenon with subsequent $N_5O_{2,3}O_{2,3}$ $(^1S_0)$ Auger decay (Kämmerling and Schmidt 1991, Kämmerling et al. 1993, Schaphorst et al. 1997), where the Auger decay is described by only one matrix element. So far, to the best of our knowledge, of all the $N_5O_{2,3}O_{2,3}$ Auger decay channels in Xenon, experimental values for the coincident angular distribution have been reported only of the $(^1S_0)$ final state. We present here the first experimental angular correlation pattern for both the Auger electron and the photoelectron while detecting the other at zero degree with respect to the polarization vector of the light for the $(^1D_2)$ and $(^3P_2)$ final states of the $N_5O_{2,3}O_{2,3}$ Auger decay process. For these final states, where more than one matrix element describes the Auger process, we were able to derive the experimental ratio of the amplitudes and the phase difference of these matrix elements. To gain access to these matrix elements, as a derivative of the angular distribution, the theoretical (PCI-included) model function was fitted to the peak intensities in the energy distributions (see figure 4a-h). The data were then integrated over the peaks with a width of 0.6 eV. The different sets of (energy) data, were scaled relative to each other using the total counts in the non-coincident spectra of the photoelectron and Auger electron lines. To account for experimental values, such as changing flux, pressure and measurement time, the total counts of the $Xe^+5p,5s$ lines in the reference detector were used. The non-coincident kinetic energy transmission function of each analyzer for the photoelectron and Auger electron was evaluated as an average value at the nominal kinetic energies. Here too, the total (non-coincident) counts recorded for the $4d_{5/2}$ line and the $4d_{5/2}(^1D_2)+4d_{3/2}(^1S_0)$ lines and $4d_{3/2}(^1D_2)+4d_{5/2}(^3P_2)$ lines (see figure 2) respectively were compared, using the theoretical angular distribution (Snell et al. 2000). Again, the coincident transmission value was evaluated by the product of the two energy transmission values of the two contributing analyzers. In order to account for the analyzer angular resolution the theoretical predictions were evaluated varying the angles by $\theta_{p,A} = 0 \pm 5^\circ$ $\phi_{p,A} = 0 \pm 5^\circ$ (see figure 1b for notation) and averaged. It turns out that the pattern of the averaged curves, vary very little from the curves for a perfect analyzer resolution.

Under the experimental condition studied here the difference between the nominal kinetic energies of the photoelectron and Auger electron is greater than the intermediate hole-state level width of $\Gamma = 120$ meV (Ausmees et al. 1995, Kämmerling et al. 1993). That allows us to describe the process in the two-step model (Scherer et al. 2001) as:

$$\begin{aligned} h\nu + Xe &\rightarrow Xe^+(4d^{-1}) + e^-_{pho}(\varepsilon l_{j_\mathrm{p}}) \\ &\hookrightarrow Xe^{2+}(4d^{10}5s^25p^4) + e^-_{Aug}(\varepsilon l_{j_\mathrm{A}}) \end{aligned}$$

In the dipole approximation the possible orbital angular momentum of the outgoing electrons $(\varepsilon j_p, \varepsilon j_A)$ is limited by the selection rule of $\Delta l = \pm 1$. The photoelectron is ejected from the d-shell, so $\varepsilon l_{j_\mathrm{p}}$ can be $\varepsilon p_{3/2}$,$\varepsilon f_{5/2}$, or $\varepsilon f_{7/2}$, and it is found (Kämmerling and Schmidt 1991, Johnson and Cheng 1992, Snell et al. 1999, Snell et al. 2001) that the εf channel is dominant near the maximum of the shape resonance of the $4d$ cross section ($h\nu \approx 100eV$) .

The Auger electron for the $N_5O_{2,3}O_{2,3}$ is ejected from the p-shell, so $\varepsilon l_{j\mathrm{A}}$ can be in general $\varepsilon s_{1/2}$ or $\varepsilon d_{3/2}$, $\varepsilon d_{5/2}$, depending upon the final state of $Xe^{2+}(4d^{10}5s^25p^4)$. For qualitative description of the triple differential cross section we choose the approach of Sheinerman and Schmidt (1997) and Scherer et al. (2001). Considering the coupling, within a jj-scheme, of the photoelectron angular and spin momenta, $\vec{l_p}+\vec{s_p}=\vec{j_p}$, then coupled to the $4d^{-1}_{J=5/2}$ hole state to get a $J_f=1$ final state (since the ground state is $J_g=0$) and the further coupling of the Auger electron angular and spin momenta, $\vec{l_A}+\vec{s_A}=\vec{j_A}$ (with $s_p=s_A=1/2$) that is finally coupled to the residual $5p^4_j$ state to produce the $4d^{-1}_{J=5/2}$ hole state, we get

$$\frac{\mathrm{d}^3\sigma_{\hat{x}}}{\mathrm{d}\theta_\mathrm{a}\mathrm{d}\theta_\mathrm{b}\mathrm{d}E} \propto \sum_{m_{s,a},m_{s,b}} \left| \frac{\sum_{j_\mathrm{p}} D_{j_\mathrm{p}} \sum_{j_\mathrm{A}} A_{j_\mathrm{A}} \mathcal{Y}^{l_\mathrm{p} m_{s,a} j_\mathrm{p}}_{l_\mathrm{A} m_{s,a} j_\mathrm{A}}(\hat{k}_\mathrm{a},\hat{k}_\mathrm{b})}{h\nu - E_I^+ - E_\mathrm{a} + i\Gamma/2} \times R(\hat{k}_\mathrm{a},\hat{k}_\mathrm{b}) + (-1)^S[\mathrm{a}\leftrightarrow\mathrm{b}] \right|^2 \tag{6}$$

where $\mathcal{Y}^{l_\mathrm{p} m_{s,a} j_\mathrm{p}}_{l_\mathrm{A} m_{s,a} j_\mathrm{A}}(\hat{k}_\mathrm{a},\hat{k}_\mathrm{b})$ are the bipolar spherical harmonics, and $R(\hat{k}_\mathrm{a},\hat{k}_\mathrm{b})$ is the correction due to PCI effect. D_{j_p} and A_{j_A} are the amplitudes of the possible photoelectron and Auger electron waves. The bipolar spherical harmonics are given by

$$\begin{aligned}\mathcal{Y}^{l_p\ m_{s,p}\ j_\mathrm{p}}_{l_A\ m_{s,A}\ j_\mathrm{A}} = \sum_{m_\mathrm{p},m_\mathrm{A}} & C^{\ l_p\ \ 1/2\ \ j_\mathrm{p}}_{m_\mathrm{p}-m_{s,p}\ m_{s,p}\ m_\mathrm{p}} C^{\ l_A\ \ 1/2\ \ j_\mathrm{A}}_{m_\mathrm{A}-m_{s,A}\ m_{s,A}\ m_\mathrm{A}} C^{\ j\ \ j_\mathrm{A}\ \ 5/2}_{-m_\mathrm{p}-m_\mathrm{A}\ m_\mathrm{A}\ -m_\mathrm{p}} C^{\ 5/2\ j_\mathrm{p}\ 1}_{-m_\mathrm{p}\ m_\mathrm{p}\ 0} \\ & \times Y_{l_p,m_\mathrm{p}-m_{s,p}}(\hat{k}_\mathrm{p}) Y_{l_A,m_\mathrm{A}-m_{s,A}}(\hat{k}_\mathrm{A})\end{aligned} \tag{7}$$

(With $j=0$ for the final states $^1S_0$ and $^3P_0$, $j=1$ for $^3P_1$, and $j=2$ for $^1D_2$ and $^3P_2$, $C^{\ j_1\ j_2\ j_3}_{m_1\ m_2\ m_3}$ are the Clebsch-Gordon coefficients $(j_1m_1\ j_2m_2|j_3m_3)$). Equation (6) reduces to equation (1) given in (Scherer et al. 2001) for the special case of the $^1S_0$ final state, since $C^{\ j\ \ j_\mathrm{A}\ 5/2}_{-m_\mathrm{p}-m_\mathrm{A}\ m_\mathrm{A}\ -m_\mathrm{p}} = 1$due to $j=0$ and further $m_p=-m_A$. The outgoing waves of the Auger electron depends on the final state of the Auger transition: only $\varepsilon d_{5/2}$ are allowed for the $^1S_0$ final state, while for the $^3P_2$ final state the Auger electron is limited to $\varepsilon d_{3/2}$ and $\varepsilon d_{5/2}$. Fortunately, this limits the number of possible parameters to be fitted to the experimental data for these two situations. But for the $^1D_2$ final state the Auger electron can have $\varepsilon s_{1/2}$,$\varepsilon d_{3/2}$, $\varepsilon d_{5/2)}$. The amplitudes of each waves are complex values of the form $D_{j_\mathrm{p}} = D_j e^{i\phi_j}$ and $A_{j_\mathrm{A}} = A_j e^{i\xi_j}$. Keeping with the notation of former reports, the magnitude of the amplitudes D_j are denoted by $D_+ = |D_{7/2}|$, $D_0 = |D_{5/2}|$, and $D_- = |D_{3/2}|$, and the same notation is used for ϕ_j. Similarly, we chose $A_+ = |A_{5/2}|$, $A_0 = |A_{3/2}|$, and $A_- = |A_{1/2}|$, the respective phases ξ_+, ξ_0, and ξ_- .

As described above, the experiments were performed for the special case where one analyzer was kept at $\theta = 0^\circ$ with respect to the polarization vector of the incident light, thus either the Auger electron or the photoelectron was detected at $\theta_{A,p} = 0^\circ$. This greatly reduces further the complexity of (6).

A further goal was to derive estimates of the relative values for amplitudes D_{j_p} and A_{j_A}. Since all amplitude are entering (6) in the form of products of $D_{j_\mathrm{p}}A_{j_\mathrm{A}}$, we can only estimate the ratio of magnitudes $\frac{D_+}{D_-}$, $\frac{D_0}{D_-}$,$\frac{A_+}{A_0}$, and $\frac{A_0}{A_-}$ and phase differences $\Delta\phi_{nm} = \phi_n - \phi_m$ and $\Delta\xi_{nm} = \xi_n - \xi_m$. The measured angular distributions of the TDCS of the photoelectron and Auger electron for the $^3P_2$ final state are shown in the top of figure 5 and for $^1D_2$ final state at the bottom.

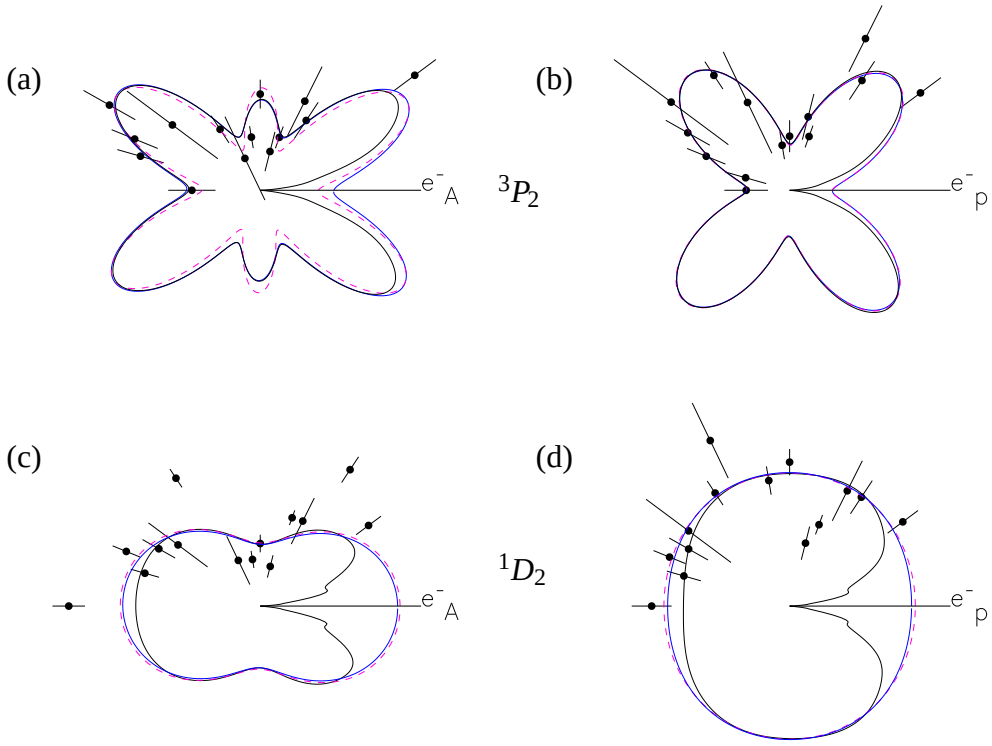

Figure 5. Polar plots of the angular distributions of the photoelectron or Auger electron. The light lines (blue in the colored version) are derived from (6) using the best fit values for each set. The (red) dashed lines show (6) using the best common fit values for all 4 distributions given in the text. The dark lines (black in the colored version) show the influence of the PCI effect and interchange effects of (3). Top($^3P_2$) final state : (a) angular distribution of the photoelectron, Auger electron ejected at 0° with respect to the photon polarization direction. (b) angular distribution of the ($^3P_2$) Auger electron.Both (a) and (b) show in general a very good agreement with the theoretical model given here. Bottom ($^1D_2$): c) angular distribution of the photoelectron, Auger electron ejected at zero degree; d) angular distribution of the Auger electron. Again, the agreement is very good.

Calculated angular distributions, without PCI effect and interchange effect, using amplitudes and phases gained by the method of (least square) fit of each data set, are shown in figure 5 as light lines (blue in the colored version). The theoretical angular distributions were scaled only in height to the experimental data. Including the PCI and possible interchange effects in the calculations results in the solid lines (black in the colored version), simulating a detector with a 0.6eV pass window. For our experimental data these effects are negligible, and our data maybe described without including both

Each pattern in figure 5 was analyzed separately and multiple fits with different starting points were performed. Due to the larger number of parameters and the fact that they appear as products in (6), a wide range of good fits to each parameter may describe our data. Also the sign of the phase differences cannot be determined within the equations. From the fit results

of the four patterns a common set of values, was chosen to describe the photoelectron in each pattern. Applying these common values to (6) results in the red) dashed curves in figure 5. We found that all four angular distributions maybe represented by $D_0/D_- = 1.1 \pm 0.3$, $D_+/D_- = 7pm5$. These are similar to the ratios of the theoretical values by Johnson and Cheng (1992) where $D_0/D_- = 1.01$, $D_+/D_- = 4.6$, and the experimental values of Snell*et al.* (2001) $D_0/D_- = 1.1$, $D_+/D_- = 4.9$. The amplitude ratio $\frac{D_+}{D_-=7pm5}$ exhibit a good agreement with the general understanding that the photoelectron is dominated by the $\varepsilon_p f_{7/2}$-wave. We further found $\Delta\phi_{0-} = 0.5 \pm 0.3$ (similar to Johnson and Cheng 1992 -0.52 to Snell*et al.* (2001) -0.65) and $\Delta\phi_{+-} = -1.4 \pm 0.3$ (compared to -0.41 and -.35 respective). In the best fit lines (blue/light curves) in figure 5 the ratio $\frac{D_+}{D_-=12pm3}$ for the $^3P_2$ distribution and $\frac{D_+}{D_-=5pm3}$.

In all four situations in figure 5 the Auger electron is characterized by a amplitude ratio of the $\varepsilon d_5/2$ to $\varepsilon d_3/2$ of $A_+/A_0 = 1.3 \pm 0.3$. The phase difference $\Delta\xi_{+0}$ was set to zero, to reduce the number of fit parameters. In addition for the $^1D_2$ final state we found ratio of $\varepsilon d_3/2$ to $\varepsilon s_1/2$ of $A_0/A_- = 1.3 \pm 0.3$ and a phase difference of $\Delta\xi_{0-} = -1.0 \pm 0.2$ These values mean that for the Auger decay the $\varepsilon_A d_{5/2}$ and $\varepsilon_A d_{3/2}$ are nearly equal and that the Auger decay to the $^1D_2$ final state the Auger electron is dominated by the $\varepsilon_A s_{1/2}$ wave.

Further improvement of the experimental uncertainty would be desirable to reduce the error of this estimated results in particular the phase differences.

Similar to (Bolognesi et al. 2004) we can use partial cross section $\sigma(4d_{5/2})$ to estimate absolute values for D_-,D_0 and D_+. One obtains the partial cross section $\sigma(4d_{5/2})$ from the matrix elements D_+, D_0, and D_- using (Huang et al. 1981)(in length form and atomic units)

$$\sigma(4d_{5/2}) = \frac{4\pi\alpha\omega}{3}\left(D_+^2 + D_-^2 + D_0^2\right) \tag{8}$$

Here α is the fine structure constant and ω the photon energy in hartree (a.u). We used (8) to normalize our amplitudes to a cross section of $\sigma(4d_{5/2}) = 12.5Mb$ (Becker et al. 1989), using the $(4d_{55/2})/(4d_{3/2})$ branching ratio of (Southworth et al. 1983). The so amplitudes are given in the last row of table **??**. The values of D_-,D_0 and D_+ are similar to the amplitudes found by Johnson and Cheng (1992). We can further test our experimental results of amplitudes and phases by calculating the angular distribution anisotropy parameter β using (Huang et al. 1981):

$$\begin{aligned}\beta(4d_{5/2}) = \quad & \left(\frac{1}{5}D_-^2 - \frac{32}{35}D_0^2 + \frac{5}{7}D_+^2 - \frac{6}{5}\sqrt{\frac{2}{7}}D_-D_0\cos\Delta_{0-}\right. \\ & \left. -12\sqrt{\frac{2}{35}}D_-D_+\cos\Delta_{+-} + \frac{12}{7}\sqrt{\frac{1}{5}}D_+D_0\cos\Delta_{0+}\right) / \left(D_+^2 + D_-^2 + D_0^2\right)\end{aligned} \tag{9}$$

and furthermore the alignment parameter $\mathcal{A}_{20}$:

$$\mathcal{A}_{20}(4d_{5/2}) = -2\left(14D_-^2 + 5D_+^2 - 16D_0^2\right) / \left(10\sqrt{14}\left(D_+^2 + D_-^2 + D_0^2\right)\right) \tag{10}$$

Note that $\mathcal{A}_{20}$ and β do not change with the normalization chosen above. With the results given at the bottom of table **??** we find $\beta(4d_{5/2}) = 0.55(35)$, and $\mathcal{A}_{20}(4d_5/2) = -0.25(15)$ which correspond well with the values of $\beta(4d_{5/2}) = 0.46$ of (Snell et al. 2000) , and $\mathcal{A}_{20}(4d_5/2) = -0.25$ of (Southworth et al. 1983, Snell et al. 2000).

4. Summary

We measured the triply differential cross section of previously unexplored doubly charged Xe^{2+} states ($^1D_2$,$^3P_2$) by coincident measurements of the $N_5O_{2,3}O_{2,3}$ Auger electrons with the $4d_{5/2}^{-1}$ photoelectron for the two final states ($^1D_2$) and ($^3P_2$) of the doubly charged ion. We found a very good agreement between our measurements and the theoretical models of the PCI effect given by both Kämmerling (1993) as well as Sheinerman and Schmidt (1997). Furthermore, the two-step model is applicable for inner electron angles θ_{12} in the range of 35° to 180° if the energy separation between the two electrons is larger than the intrinsic level width of the intermediate state. Moreover, we measured the first angular distribution pattern of the TDCS for these two final states and were able to reproduce them by a semi empirical model which describes the transitions populating these two states in the non-relativistic dipole approximation. We found that for the ($^1D_2$) final state the ratio of the amplitudes of the outgoing s-wave and the two d-waves may be described by $R = A_{j_A=1/2}/A_{j_A=3/2,5/2} = 20 \pm 10$ with $\Delta = \xi_{j_A=1/2} - \xi_{j_A=3/2,5/2} = 1.0 \pm .4$ rad. Evaluating the angular distribution of the $^3P_2$ final state we can approximated the ratio $R = A_{j_A=5/2}/A_{j_A=3/2} = 1.3 \pm 0.3$, a similar result was obtained from evaluating the ($^1D_2$) final state. The photoelectron is dominated by a $f_{7/2}$ waves, but the values found are similar to the previously reported (Johnson and Cheng 1992, Snell *et al* 2001).

5. Acknowledgment

This work has been funded by Department of Energy, Office of Science, Office of Basic Energy Sciences, Chemical Sciences, Geosciences and Biosciences Divisions. The ALS is funded by the Director, Office of Science, of the U.S. Department of Energy. We thank the Deutsche Forschungsgemeinschaft for partial support. The author is especially grateful to John Bozek at the ALS for his excellent help and support during the performance of the experiments, and the ALS staff.

Appendix A: Theoretical description of the Post collision interaction

To characterize the angular dependencies of the PCI-effect on the line shape ($|R(p,A)|^2$) as presented here, one may use either the approximate form given by Kämmerling *et al* (Kämmerling et al. 1993) or the description given by Sheinerman and Schmidt (Sheinerman and Schmidt 1997). We have found that for our experimental data range of angles between two detectors ($\theta_1 2 = 35^\circ \rightarrow 180^\circ$) and where the energy difference between Auger electron and photoelectron is much greater than the FHWM of the intermediate state both models give no visible difference in the characterization of the PCI distorted line shapes and the shift of the positions.

In the theoretical description given by Kämmerling (1993) the triply-differential cross section

is given by:

$$TDCS = \frac{d^2\sigma}{d\theta_1 d\theta_2}\frac{\Gamma}{2\pi}\frac{1}{(\varepsilon_A - E_p^0)^2 + (\Gamma/2)^2} K\left(\frac{C(r_1(t), r_2(t), \theta_{12})}{v_1}, \varepsilon_A - E_{Aug}^0\right). \tag{A.1}$$

This results in a Lorentzian profile at $\varepsilon_A = E_{Aug}^0$ when the factor $K \equiv 1$, else K will give rise to the asymmetries in the TDCS. The approximation made here is that the post-collision interaction effect between the two emitted electrons (labeled 1,2), which is dependent on the Coulomb potentials between the two electrons and the doubly charged ions, is described in terms of constant velocities of the two emitted electrons (van der Straaten et al. 1988, Kuchiev and Sheinerman 1986), and not by functions of $r_1(t)$ and $r_2(t)$. A necessary condition for this approximation of C is that $(h\nu - E_{bin}^+)^2 \geq 100 \times \Gamma$, which for the case reported here of photon energy $h\nu = 97.45$ eV, binding energy of the inner shell ionization $E_{bin}^+ = 67.5$ eV (King et al. 1977) and $\Gamma = 0.12$ eV (Ausmees et al. 1995) is well justified. Also it is assumed that the electrons are emitted on a straight path, hence the relative angle θ_{12} between the two ejected electrons remains constant during their path to the detectors.

$$C(r_1, r_2, \theta_{12}) = 1 - \frac{r_1}{|r_1 - r_2|} \tag{A.2}$$

$$C(r_1, r_2, \theta_{12}) \approx 1 - \frac{v_1}{|v_1 - v_2|} \tag{A.3}$$

with the velocities v_1 and v_2 in a.u. :

$$v_1 = \sqrt{2m_0 E_{pho}^0} \qquad v_2 = \sqrt{2m_0 E_{Aug}^0} \tag{A.4}$$

Then the post-collision interaction can be approximated, according to Kämmerling *et al* (Kämmerling et al. 1993), by

$$K(v_1, v_2, \theta_{12}) = \frac{\pi C(v_1, v_2, \theta_{12})}{\sinh(\pi C(v_1, v_2, \theta_{12}))} \exp\left[2\frac{C(v_1, v_2, \theta_{12})}{v_1} \tan^{-1}\left(\pi \frac{2(h\nu - E_{bin}^+ - \varepsilon_1)}{\Gamma}\right)\right] \tag{A.5}$$

Note: A negative factor $C(v_1, v_2, \theta_{12})$, as for small relative angle θ_{12}, gives rise to an energy gain of the photoelectron, while a positive value leads to a gain in kinetic energy of the Auger electron.

Sheinerman and Schmidt (Sheinerman and Schmidt 1997) present a model of the PCI-effect which should be used when studying cases where the angle between two detectors is very small and especially when the two particles have very similar kinetic energies and interference effects have to be considered. The factor representing PCI-effects $R(A,B)$ in (3) is given by (using the following notation: A=photoelectron, B=Auger electron, C the doubly charged ion, and D the intermediate singly charged ion):

$$R(A,B) = \exp(-\pi\xi/2)\Gamma(1-a)\Gamma(b)\left(\varepsilon_B - \varepsilon_{Aug}^0 + i\frac{\Gamma}{2}\right)^{1-b} \times {}_2F_1(a,b,1,z) \tag{A.6}$$

with the parameters and $V_{ij} = V_i - V_j$ and $\boldsymbol{K_{ij}} = \frac{1}{2}\boldsymbol{V_{ij}}$

$$\xi = \xi_{AB} + \xi_{AC} - \xi_{AD} \qquad \texttt{where}\ \xi_i j = z_i z_j / \left(V_{ij}\right) \tag{A.7}$$

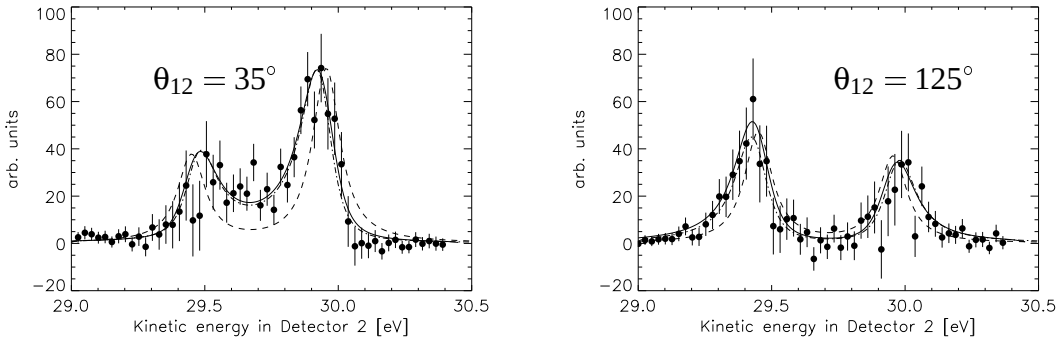

Figure A1. TDCS of the final state $(^1S_0)$ at a photon energy of $h\nu = 97.0$ eV at $\theta_{12} = 35°$ and 125°. Theoretical curves: dot dashed line: according to (A.1), dashed line: TDCS without PCI and interchange effects, solid line: according to (3). The slightly higher intensity at $\theta_{12} = 35°$ where $\varepsilon_p = \varepsilon_A$ is due to PCI-induced interference.

${}_2F_1(a,b,1,z)$ is the full hypergeometric function with its parameters and arguments:

$$a = -i\xi_{AB}, \qquad b = 1 + i(\xi_{AC} - \xi_{AD}) \qquad z = -\frac{(K_{AB}\kappa/\mu_{AD} + \boldsymbol{K_{AB}} \cdot \boldsymbol{V_{AD}})}{\left(\varepsilon_p - \varepsilon^0_{Aug} + i\frac{\Gamma}{2}\right)} \tag{A.8}$$

wherein $\kappa = \left(2\varepsilon^0_{pho} + i\Gamma\right)^{1/2}$. Again in the analysis of the data presented here, both models give very similar result. However it must be stated clearly, that (A.5) is only valid for cases were the difference of kinetic energy $\Delta E = \varepsilon_1 - \varepsilon_2 >> \Gamma$ or larger angle of θ_{12}.

As stated before, if ΔE and the angle between the two emitted electron both becomes small the PCI effects are such that a considerable overlap in energy of the two electrons will occur. This will lead to interference effects between the photoelectron and Auger electrons and (A.5) becomes invalid. At the left side of figure A1 for the case of $\theta_{12} = 35°$, the influence of the interference effect, although very small at this configuration, leads to a stronger TDCS between the two peaks. Here the enhanced description of the factor $R(a,b)$ given by Sheinerman and Schmidt (Sheinerman and Schmidt 1997) should be used. On the other hand the data for $\theta_{12} = 125°$ is well described by the theoretical model used here. This is due to the fact that the PCI effect leads to a further separation of the two electrons; hence interference effects become even less likely. In summary, we would like to note that when using (A.1) through A.5 one must be aware of the experimental conditions.

References

Åberg T 1980 *Phys. Scr.* **21**, 495.

Åberg T and Howard G 1982 *Corpuscules and Radiation in Matter, Encyclopedia of Physics*, ed W Mehlhorn.

Armen G B, Sorensen S L, Whitfield S B, Ice G E, Levin J, Brown G S and Crasemann B 1987 *Phys. Rev. A* **35**, 3966.

Ausmees A, Osborne S J, Moberg R, Svensson S, Aksela S, Sairanen O P, Kivimki A, Naves de Brito A, Nõmmiste E, Jauhiainen J and Aksela H 1995 *Phys. Rev. A* **51**, 855.

Avaldi L and Huetz A 2005 *J. Phys. B: At. Mol. Phys.* **38**, S861.
Becker U, Szostak D, Kerkhoff H G, Kupsch M, Langer B, Wehlitz R, Yagishita A and Hayaishi T 1989 *Phys. Rev. A* **39**, 3902.
Bolognesi P, De Fanis A, Coreno M, and Avaldi L 2004 *Phys. Rev. A* **70**, 022701.
Borst M and Schmidt V 1986 *Phys. Rev. A* **33**, 4456.
Briggs J S and Schmidt V 2000 *J. Phys. B: At. Mol. Opt. Phys.* **33**, R1.
Dörner R, Bräuning H, Feagin J M, Mergel V, Jagutzki O, Spielberger L, Vogt T, Khemliche H, Prior M H, Ullrich J, Cocke C L and Schmidt-Böcking H 1998 *Phys. Rev. A* **57**, 1074.
Huang K N, Johnson W R and Cheng K T 1981 *At. Data Nucl. Data Tables* **26**, 33.
Johnson W R and Cheng K T 1992 *Phys. Rev. A* **46**, 2952.
Kämmerling B and Schmidt V 1991 *Phys. Rev. Lett.* **67**, 1848.
Kämmerling B, Krässig B and Schmidt V 1993 *J. Phys. B: At. Mol. Opt. Phys.* **26**, 261.
King G, Tronc M, Read F H and Bradford R C 1977 *J. Phys. B: At. Mol. Phys.* **18**, 2479.
Kuchiev M Y and Sheinerman S A 1986 *Sov. Phys.-JETP* **19**, L85.
Kuchiev M Y and Sheinerman S A 1989 *Sov. Phys.-Usp* **32**, 569.
Lablanquie P, Sheinerman S, Penet F, Hall R I, Ahmad M, Hikosaka Y and Ito K 2001 *Phys. Rev. Lett.* **87**, 053001.
Lörch H, Scherer N, Kerkau T and Schmidt V 2001 *J. Phys. B: At. Mol. Opt. Phys.* **34**, 3963.
Lohman B 1996 *Aust. J. Phys* **49**, 365.
Maulbetsch F and Briggs J S 1995 *J. Phys. B: At. Mol. Opt. Phys.* **28**, 551.
Mazeau J, Selles P, Waymel D and Huetz A 1991 *Phys. Rev. Lett.* **7**, 820.
NIST *Atomic Spectra Database Energy levels Data* online at
`"http://physics.nist.gov/PhysRefData/ASD/levels_form.html"`
Rioual S, Rouvellou B, Avaldi L, Baretta G, Camilloni R, Stefani G and Turri G 2001 *Phys. Rev. Lett.* **862**, 1470.
Schaphorst S J, Jean A, Schwarzkopf O, Lablanquie P, Andric L, Huetz A, Mazeau J and Schmidt V 1996 *J. Phys. B: At. Mol. Opt. Phys.* **29**, 1901.
Schaphorst S J, Qian Q, Krässig B, van Kampen P, Scherer N and Schmidt V 1997 *J. Phys. B: At. Mol. Opt. Phys.* **30**, 4003.
Scherer N, Lörch H, Kerkau T and Schmidt V 1999 *Phys. Rev. Lett.* **82**, 4615.
Scherer N, Lörch H, Kerkau T and Schmidt V 2001 *J. Phys. B: At. Mol. Opt. Phys.* **34**, L339.
Scherer N, Lörch H, Kerkau T and Schmidt V 2004 *J. Phys. B: At. Mol. Opt. Phys.* **37**, L121.
Schmidt V 1999 *J. Physique IV* France, Int. Conference on Coincidence Spectroscopy **9**, 75.
Schmidt V, Krummacher S, Wuilleumier F and Dhez P 1981 *Phys. Rev. A* **24**, 1803.
Schwarzkopf O and Schmidt V 1996 *J. Phys. B: At. Mol. Opt. Phys.* **29**, 3032.
Schwarzkopf O, Krassig B, Elminger J and Schmidt V 1993 *Phys. Rev. Lett.* **70**, 3008.
Selles P, Mazeau J, Lablanquie P, Malegat L and Huet A 1998 *J. Phys. B: At. Mol. Opt. Phys.* **31**, L353.
Sheinerman S A and Schmidt V 1997 *J. Phys. B: At. Mol. Opt. Phys.* **30**, 1677.
Snell G, Langer B, Drescher M, Müller N, Zimmermann B, Hergenhahn U, Viefhaus J, Heinzmann U and Becker U 1999 *Phys. Rev. Lett.* **82**, 1480.
Snell G, Kukk E, Langer B and Berrah N 2000 *Phys. Rev. A* **61**, 042709.
Snell G, Hergenhahn U, Müller N, Drescher M, Viefhaus J, Becker U, and Heinzmann U 2001 *Phys. Rev. A* **63**, 0432712.
Southworth S, Becker U, Truesdale C M, Kobrin P H, Lindle D W, Owaki S and Shirley D A 1983 *Phys. Rev. A* **31**, 261.
Tulkki J, Armen G B, Aberg T, Crasemann B and Chen M H 1987 *Z. Phys. D* **5**, 241.
van der Straten P, Morgenstern R and Niehaus A 1988 *Z. Phys. D* **8**, 35.
Vegh L and Macek J H 1994*a Phys. Rev. A* **50**, 4031.
Vegh L and Macek J H 1994*b Phys. Rev. A* **50**, 4036.
Viefhaus J, Avaldi L, Heiser F, Hentges R, Gessner O, Rúdel A, M. Wiedenhoeft K W and Becker U 1996 *J. Phys. B: At. Mol. Opt. Phys.* **29**, L729.
Viefhaus J, Braune M, Korica S, Reinkster A, Rolles D and Becker U 2005 *J. Phys. B: At. Mol. Phys.* **38**, 3885.

Viefhaus J, Cvejanovic S, Langer B, Lischke T, Prmper G, Rolles D, Golovin A V, Grum-Grzhimailo A N, Kabachnik. N M and Becker U 2004 *Phys. Rev. Lett.* **92**, 083001.

Viefhaus J, Snell G, Hentges R, Wiedenhoeft M, Heiser F, Gessner O and Becker U 1998 *Phys. Rev. Lett.* **80**, 1618.

Wuilleumier F and Krause M 1979 *J. Electron. Spectrosc. Relat. Phenom* **15**, 15.